Graphical Abstract

Reevaluating the fate of subducted magnesite in the Earth's lower mantle.

Lélia Libon, Georg Spiekermann, Ingrid Blanchard, Johannes M. Kaa, Serena Dominijanni, Melanie J. Sieber, Mirko Förster, Christian Albers, Wolfgang Morgenroth, Catherine McCammon, Anja Schreiber, Vladimir Roddatis, Konstantin Glazyrin, Rachel J. Husband, Louis Hennet, Karen Appel, Max Wilke

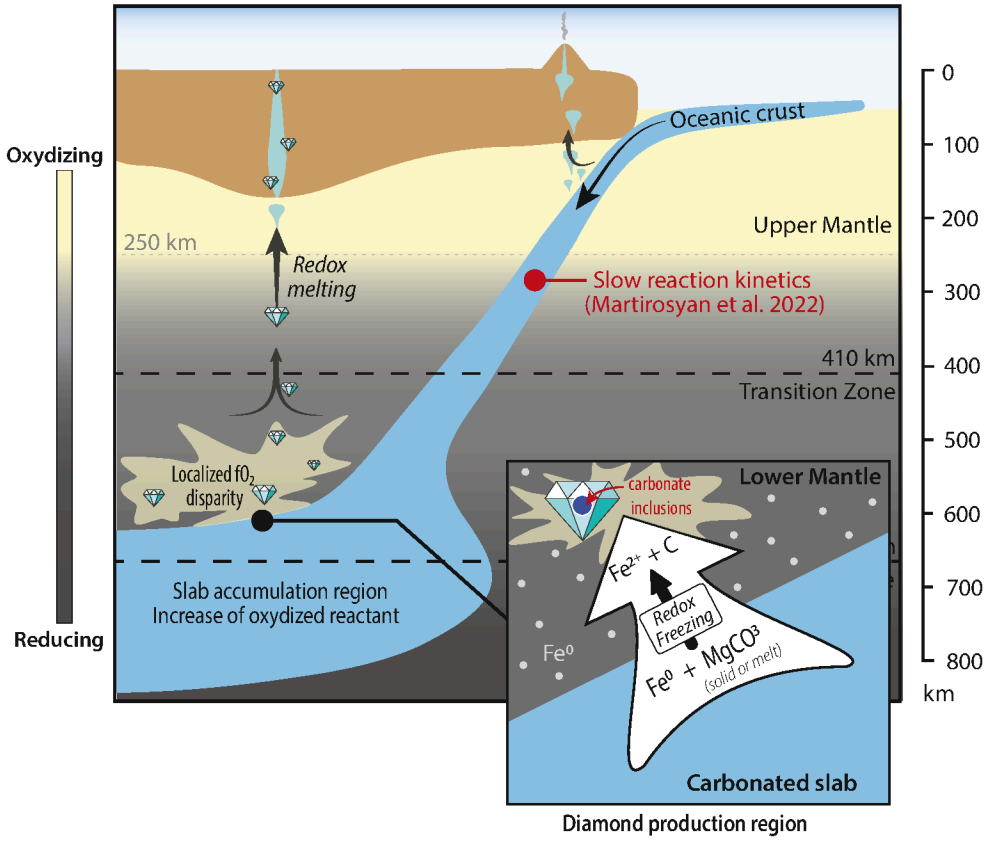

Highlights

Reevaluating the fate of subducted magnesite in the Earth's lower mantle.

Lélia Libon, Georg Spiekermann, Ingrid Blanchard, Johannes M. Kaa, Serena Dominijanni, Melanie J. Sieber, Mirko Förster, Christian Albers, Wolfgang Morgenroth, Catherine McCammon, Anja Schreiber, Vladimir Roddatis, Konstantin Glazyrin, Rachel J. Husband, Louis Hennet, Karen Appel, Max Wilke

- The stability of magnesite ($MgCO_3$) was investigated in the presence of iron-bearing bridgmanite at conditions from 25 to 68 GPa and temperatures covering all subduction geotherms (1350 K to 2000 K).
- Magnesite reacts with iron-bearing bridgmanite to form diamonds at conditions relevant to the coldest geotherm.
- Subduction of magnesite, and more generally carbonates, is limited to the top of the lower mantle (∼700 km depths), even along cold slabs geotherm.

Reevaluating the fate of subducted magnesite in the Earth's lower mantle.

Lélia Libon[a,1,*], Georg Spiekermann[b], Ingrid Blanchard[c,a], Johannes M. Kaa[d,e], Serena Dominijanni[c,f], Melanie J. Sieber[a], Mirko Förster[a], Christian Albers[e], Wolfgang Morgenroth[a], Catherine McCammon[f], Anja Schreiber[g], Vladimir Roddatis[g], Konstantin Glazyrin[h], Rachel J. Husband[h], Louis Hennet[i], Karen Appel[d], Max Wilke[a]

[a]*Institute of Geosciences, University of Potsdam, Karl-Liebknecht-Str. 24-25, Potsdam, Golm, 14476, Germany*
[b]*Institute of Mineralogie, University of Münster, Corrensstraße 24, Münster, 48149, Germany*
[c]*Institut de Minéralogie, de Physique des Matériaux et de Cosmochimie (IMPMC), Sorbonne Université, Paris, 75252, France*
[d]*European X-Ray Free-Electron Laser Facility GmbH, Holzkoppel 4, Schenefeld, 22869, Germany*
[e]*Fakultät Physik/DELTA, Technische Universität Dortmund, Dortmund, 44227, Germany*
[f]*Bayerisches Geoinstitut, Universität Bayreuth, Bayreuth, 95440, Germany*
[g]*Deutsches GeoForschungsZentrum GFZ, Telegrafenberg, Potsdam, 14473, Germany*
[h]*Deutsches Elektronen-Synchrotron DESY, Notkestr. 85, Hamburg, 22607, Germany*
[i]*ICMN, CNRS - Université d'Orléans, 1b rue de la Férollerie, Orléans, 45071, France*

Abstract

The role that subducted carbonates play in sourcing and storing carbon in the deep Earth's interior is uncertain, primarily due to poor constraints on the stability of carbonate minerals when interacting with mantle phases. Magnesite ($MgCO_3$) is the most prominent carbonate phase to be present at all mantle pressure-temperature conditions. In this study, we combined

*Corresponding author
[1]now at Institut de minéralogie, de physique des matériaux et de cosmochimie (IMPMC), Sorbonne University, Paris, France

multi-anvil apparatus and laser-heated diamond anvil cell experiments to investigate the stability of magnesite in contact with iron-bearing bridgmanite. We examined the presence of melt, decarbonation, and diamond formation at shallow to mid-lower mantle conditions (25 to 68 GPa; 1350 to 2000 K). Our main observation indicates that magnesite is not stable at shallow lower mantle conditions. At 25 GPa and under oxidizing conditions, melting of magnesite is observed in multi-anvil experiments at temperatures corresponding to all geotherms except the coldest ones. Whereas, at higher pressures and under reducing conditions, in our laser-heated diamond-anvil cell experiments, diamond nucleation is observed as a sub-solidus process even at temperatures relevant to the coldest slab geotherms. Our results indicate that magnesite was reduced and formed diamonds when in contact with the ambient peridotite mantle at depths corresponding to the shallowest lower mantle (33 GPa). Thus, we establish that solid magnesite decomposes at depths of ∼700 km as it contacts the ambient mantle. Consequently, the recycling of carbonates will hinder their transport deeper into the lower mantle.

Keywords: Deep carbon cycle, Lower mantle, Carbonates, Diamond formation, Decarbonation

---

1. Introduction

Over geologic time, carbon moved between surface and deeper reservoirs, impacting the atmospheric, oceanic, and crustal CO_2 budget (Plank and Manning, 2019; Kelemen and Manning, 2015). The carbonates entrapped in subducting slabs have significant potential to transport carbon from the

Earth's surface to its deep interior. The flux of carbon reaching the deep mantle beyond the volcanic arc remains highly uncertain, with estimates broadly ranging from 0.0001 to 52 Mt of C per year (Kelemen and Manning, 2015). This uncertainty largely stems from a limited understanding regarding the survival of carbonate minerals during their transport to deep mantle conditions. Indeed, carbonates contained within oceanic crust sediments are expected to be recycled beneath the volcanic arc, with carbon returning to the surface environment through volcanic degassing and magmatism. Current constraints suggest that a significant amount of carbonates may survive the first 150 km of subduction and make it deeper into the Earth's deep mantle (Molina and Poli, 2000; Connolly, 2005; Gorman et al., 2006; Kerrick and Connolly, 2001).

Transport of carbonates to at least the transition zone has been proposed based on the presence of carbonate inclusions in super-deep diamonds (Brenker et al., 2007; Kaminsky et al., 2016; Wirth et al., 2009). Such diamonds originate from depths greater than 250 km, and provide direct insight into the deep carbon reservoir. As subducted carbonates may provide an appreciable contribution of carbon to the deep mantle, it is imperative to thoroughly explore the stability of carbonate minerals from upper to lower mantle conditions.

In order to "survive" subduction to the deep mantle, carbonates must avoid re-mobilizing processes such as melting and decarbonation. Investigations on melting temperatures of carbonated oceanic crust have been central to better understand the behavior of deeply subducted oceanic crust and surrounding mantle. Deeply subducted carbonates decrease the melting tem-

perature of mantle peridotite by several hundreds of degrees (Dasgupta and Hirschmann, 2006; Brey et al., 2008; Litasov and Ohtani, 2009; Ghosh et al., 2009). Previous experimental studies have constrained the melting temperature of carbonated peridotite (∼1950 K at 23 GPa) and carbonated MORB (∼1450 K at 20 GPa) and identified a barrier for carbonate subduction at transition zone depths due to melting (Thomson et al., 2016b; Rohrbach and Schmidt, 2011; Kiseeva et al., 2013). When oxidized carbonate-rich melts are released into the surrounding reduced mantle at depths greater than 250 km, they are unstable and get reduced to form diamonds (Rohrbach and Schmidt, 2011). This is also evidenced by carbon isotope composition of sublithospheric diamonds and their mineral inclusions (Walter et al. (2022) and references therein). Indeed, the stabilization of a (Fe, Ni)-metal phase beyond ∼250 km depths, due to the disproportionation of FeO into Fe_2O_3 + Fe^{metal} (Fe^0) (Frost et al., 2004; Rohrbach et al., 2007; Frost and McCammon, 2008), constrains the mantle's oxygen fugacity (fO_2) at values around the iron-wüstite (IW) buffer. Such conditions impose a relative buffering capacity within the deep mantle that favors the reduction of carbonates and carbonated melts to form diamonds through the 'redox freezing' reaction (Eq.1) (Rohrbach and Schmidt, 2011; McCammon et al., 2020):

$$\underset{\text{solid}}{2\text{Fe}} + \underset{\text{solid or melt}}{\text{MgCO}_3} \longrightarrow 3(\underset{\text{solid}}{\text{Fe}_{2/3}, \text{Mg}_{1/3}})\text{O} + \underset{\text{solid}}{\text{C}} \tag{1}$$

Accordingly, 'redox freezing' provides an effective mechanism for diamond crystallization across the mantle at depths from ∼250 to ∼700 km, and contributes to the barrier that hinders carbonate transport into the deep Earth (Thomson et al., 2016b; Rohrbach and Schmidt, 2011).

Despite evidence for a melting barrier that limits the preservation of subducted carbonates, it has been proposed that solid carbonates may bypass melting and reach the lower mantle if carried in cold subducting slabs (Thomson et al., 2016b, 2014; Kiseeva et al., 2013). Among those carbonates, magnesite ($MgCO_3$) is the most likely carbonate phase to be preserved within subducted oceanic crust that reaches the lower mantle due to (1) its production during the transformation of major carbonates (dolomite and calcite/aragonite) at pressure conditions from 3 to 9 GPa (Yaxley and Brey, 2004; Sato and Katsura, 2001; Luth, 2001) and (2) as a single phase magnesite and its high-pressure polymorph ($MgCO_3$-II) are stable as solid phases throughout all pressure and temperature conditions of the Earth's mantle (Binck et al., 2020; Isshiki et al., 2004; Solopova et al., 2015).

Experimental investigations have shown that magnesite is the preferred stable carbonate in contact with $CaSiO_3$ up to ∼80 GPa (Biellmann et al., 1993; Lv et al., 2021). However, magnesite may become unstable as it reacts with SiO_2 to form diamonds or CO_2 + $MgSiO_3$ even at sub-solidus temperatures (Drewitt et al., 2019; Maeda et al., 2017; Takafuji et al., 2006; Litasov and Shatskiy, 2019; Koziol and Newton, 1995; Kakizawa et al., 2015; Seto et al., 2008). Most recently, Drewitt et al. (2019) proposed that the deepest plausible carbon survival barrier exists at mid-lower mantle depths (∼60 GPa) under very cold subduction geotherm conditions. The authors observed the decarbonation of magnesite in the absence of melting in laser-heated diamond anvil cell (LH-DAC) experiments. However, carbonates entering the lower mantle (≥660 km) will encounter reducing conditions with a considerable buffering capacity, as the lower mantle is expected to contain an

average of ∼1 wt% metallic-Fe (Fe^0) (Frost and McCammon, 2008). Whereas previous studies have primarily considered simplified iron-free systems with magnesite reacting with free SiO_2, the role of iron in carbonate-silicate interactions remains unclear. Even when iron (as FeO) has previously been included in the experimental system (e.g., Drewitt et al. (2019)), its potential to influence redox-sensitive phases such as carbonates, as well as its elemental partitioning was not discussed. Subducted carbonates will be in contact with metallic iron as they reach the lower mantle. In an effort to model such redox interactions, experimental investigations of the $MgCO_3$ + Fe^0 reaction were conducted at lower mantle conditions, revealing that magnesite's redox-breakdown is a viable sub-solidus mechanism to form diamonds (Dorfman et al., 2018; Martirosyan et al., 2019; Zhu et al., 2019). To thoroughly understand the transportation of carbonates in the deep Earth, experimental studies of multi-component, natural-like systems are required at controlled pressure and temperature and defined redox conditions (Stagno et al., 2019).

This study further explores the fate of magnesite subducted into the lower mantle. We examine the stability of magnesite in co-existence with the most abundant lower mantle mineral, bridgmanite $(Mg, Fe)SiO_3$. In particular, we assess the processes of decarbonation, melting, and diamond formation at lower mantle conditions, in which Fe is likely to play a crucial role. We conducted high-pressure experiments with two experimental techniques: (1) large-volume press experiments using multi-anvil apparatuses were conducted to better assess the presence of melt at the top of the lower mantle (25 GPa and 1600 to 2000 K), and (2) LH-DAC experiments were conducted to assess

the magnesite-silicate interaction over a wider range of pressures (from top to mid-lower mantle conditions; 33 to 75 GPa) and temperatures (covering all subduction geotherms; 1300 to 2000 K). Our system aims to serve as an analog for reactions that occur between the mantle and carbonated subducted slabs.

2. Material and methods

2.1. Starting materials

All experiments started with natural magnesite ($Mg_{0.99}Ca_{0.01}CO_3$) (<0.5 wt% of trace elements) (Table 1) mixed with a silicate reactant. Three magnesite-silicate mixtures were used as starting materials: (1) MG11 = magnesite + silicate glass in a 1:1 ratio (14 pressure-temperature points) (2) MG13 = magnesite + silicate glass in a 1:3 ratio (2 pressure-temperature points) and (3) MO11 = magnesite + olivine in a 1:1 ratio (4 pressure-temperature points). Our synthetic silicate glass used in MG11 and MG13 was synthesized at ICMN (Orléans, France) by the aerodynamic levitation technique (Hennet et al., 2002; Auzende et al., 2011). The composition of $Mg_{0.8}Fe_{0.2}SiO_3$ (Table 1), was purposefully designed for this study to reflect a typical composition of bridgmanite. Argon (99.999% 2-3 ppm O_2) was used as a levitating gas to ensure a reducing atmosphere at around log $fO_2 \sim$ -5.5 to minimize the amount of ferric iron in the glass but the content of ferric iron in the synthetic glass was not analyzed.

However, using the calibration of O'Neill et al. (2018) and temperature of 1600 °C a $Fe^{3+}/\sum Fe \leq 0.03$ can be estimated. In MO11 mixture, single crystals of olivine ($Mg_{1.82}Fe_{0.17}SiO_4$) was used. In addition, for multi-anvil

experiments, two silicate glasses were synthesized with the same stoichiometric composition but doped with either Sr or La (∼4000 ppm and ∼5600 ppm, respectively, Table 1) and will be referred as MG11:Sr and MG11:La. The addition of these incompatible elements (Sr and La) served to trace the presence of melt in our experiments.

wt%	magnesite (15)	glass (25)	Sr:glass (60)	La:glass (17)	olivine (10)
SiO_2	-	55.51(0.30)	57.47(0.36)	58.55(0.35)	40.87(0.18)
Al_2O_3	-	0.42(0.03)	0.45(0.03)	0.45(0.04)	-
FeO	0.05(0.03)	13.71(0.28)	13.48(0.36)	12.04(0.33)	8.23(0.10)
MgO	46.95(0.56)	29.37(0.24)	27.40(0.23)	27.85(0.36)	49.10(0.21)
CaO	0.92(0.32)	-	-	-	0.06(0.004)
MnO	0.01(0.01)	-	-	-	0.12(0.02)
CO_2 [a]	51.97(0.37)	-	-	-	-
SrO	-	-	0.67(0.07)	-	-
La_2O_3	-	-	-	0.48(0.07)	-
Total		99.01	99.47	99.37	98.38
Mg#	-	79.3	78.4	80.5	91.4

Table 1: Chemical composition of starting materials measured by EPMA (wt%). Numbers in parentheses next to the phase names are the number of analyses averaged. The number in parentheses next to the measurement refers to the standard deviation (1σ). [a]Calculated from the total deficit from the analyses. Mg# = [Mg/(Mg+Fe+Ca)]×100

.

For LH-DAC experiments, approximately 10 wt.% of Pt-black (platinum powder) was added to only MO11 as a laser coupler, but not for the other compositions (MG13 and MG11). All starting materials were powder mix-

tures ground in an agate mortar with acetone for 20 minutes to achieve homogenization and to ensure a grain size <5 µm. Each starting material was checked before mixing by electron microprobe (EPMA) and kept in an oven (∼120-150 °C) to limit the absorption of atmospheric water over time.

2.2. High-pressure and high-temperature experiments and analyses

Two high-pressure devices were used: (1) the multi-anvil apparatus allowed for large sample volume and investigation of quenched run products by EPMA and scanning electron microscopy (SEM). (2) LH-DAC offered in situ characterization through the transparent diamond windows, at the expense of sample size.

2.2.1. Multi-anvil apparatus experiments

Experiments were conducted at 25±1 GPa and 1600-2000±100 K for 1 to ∼2 hours (Table 2) using a Hymag 1000t and a Sumitomo 1200t multi-anvil apparatus installed at the Bayerisches Geoinstitut (BGI, Germany). Tungsten carbide (WC) anvils of 3 mm truncation edge length (TEL) were used with a 7 mm edge length Cr_2O_3-doped MgO octahedron (OEL), referred to as 7/3 (OEL/TEL) assembly. The starting materials were either MG11:Sr (Exp. #4 and #7) or MG11:La (Exp. #4b, #5, #6 and #9) enclosed in ∼1 mm × ∼0.8 mm (length × diameter) folded rhenium capsules to prevent Fe loss. High temperatures were achieved with a cylindrical $LaCrO_3$ heater and kept constant within ±20 °C. Temperatures were estimated either with D-type thermocouples ($W_{97\%}Re_{3\%}$-$W_{75\%}Re_{25\%}$) placed horizontally through the wall of the furnace in direct contact with the capsule, or by the heating power (W) versus temperature (°C) calibration with an accuracy of ±100 °C

(Keppler and Frost, 2005). Each experiment contained one capsule except for run #4 in which two capsules (#4a and #4b) were placed in one assembly. More details on the cell assembly can be found in Fig. S**??**. The samples were quenched by switching off the electrical power and then decompressed to ambient pressure overnight (∼15 hours). After the experiments, the recovered samples were mounted in epoxy, polished using diamond sprayed aluminum pads at BGI, and then, carbon-coated, and examined at the University of Potsdam for textural features with SEM (Fig. 1A) and for major element compositions with an EPMA JEOL JXA-8200. A 15 keV and 15 nA beam and a ZAF matrix correction were used. The beam diameter varied depending on the phases being analyzed; 2 µm for silicate minerals, 5 µm for carbonate minerals, and 5 to 7 µm for average melt composition measured in the dendritic quenched-melt (QM) texture. The EPMA standards used for silicate phase measurements were either garnet and diopside or clinopyroxene and orthopyroxene for Al, Fe, Mg, Ca, and Si, albite for Na, strontianite for Sr, and lanthanum-phosphate for La. For the carbonate phase and quenched melt measurements, standards were dolomite for Ca and Mg, siderite for Fe, strontianite for Sr, lanthanum-phosphate for La, and albite for Na. CO_2 concentrations were not quantified but calculated from the deficit of the analytical totals (Table S**??**).

2.2.2. Laser-heated diamond anvil cell experiments

LH-DAC experiments were performed from 33 to 75 GPa and 1300 to 2050 K using BX90 diamond anvil cells (Kantor et al., 2012) and diamond anvils of 300 or 200 µm culets depending on the target pressure. Rhenium gaskets were indented to a thickness of 35 to 45 µm and then drilled to

produce sample chambers from 80 to 130 µm in diameter. Compressed 15 to 20 µm thick starting material platelets with a diameter equivalent to the ones of the sample chambers were loaded between two layers of NaCl to isolate our sample from the diamond anvils, and to limit C diffusion. One experiment without magnesite (ON34), containing only a compressed platelet of silicate glass in between insulating NaCl layers, was carried out at 43 GPa and 1300 K to investigate the run products issued from the glass crystallization itself. Each cell was placed in an oven at ∼120-150 °C overnight prior to compression to minimize water absorption before closing. The experimental conditions and run products of each experiment are reported in Table S**??**.

The pressure was determined before and after laser heating using the shift of the Raman peak of the diamond anvil at the culet (Hanfland et al., 1986) using the calibration scale of Akahama and Kawamura (2006) with a measurement accuracy of ±2 GPa and verified using the equation of state of the NaCl pressure medium (Fei et al., 2007) after heating. Reported pressures are those measured from the diamond anvil post-heating, which typically differed by <4 % to the pre-heating pressure. Pressure measured from the NaCl medium differed by ±2 GPa from the diamond anvil post-heating pressure. No corrections were made for thermal pressure during heating, but the pressure during laser heating may be estimated to be about 10% higher than the pre-heating pressure at the modest temperatures achieved in this study (Fiquet et al., 2010).

Synchrotron in situ X-ray diffraction (XRD) measurements were carried out at the Extreme Conditions Beamline (ECB, P02.2) at PETRA III, in Hamburg (Germany) (Liermann et al., 2015). High-temperature condi-

tions were achieved by using a double-sided YAG fiber laser emitting at 1072 nm with a Gaussian shape and a spot size of 20 µm (FWHM) which was co-aligned to a micro-focused X-ray beam of 1.5 × 1.5 µm^2 (FWHM) (Konôpková et al., 2021). Two beam shapers are equipped on each side of the laser heating system, which enables independent shaping of the focal spot and are intended to ensure a flat-top intensity distribution of the laser-focused beam. The high temperature was held stable for 5 to 36 minutes, after which the sample was quenched by turning off the laser emission. The temperature was measured radiospectrometrically during heating in the center of the hot spot by fitting a grey body distribution to the measured thermal radiation spectra in the spectral range between 640 to 850 nm. The temperature error is 10% of the temperature value at ECB, which includes temperature gradients, heating instabilities due to fast changes in optical properties from the sample, and signal sensitivity (Konôpková et al., 2021). The reported temperatures are the temporal average of the temperature measurements series over the heating duration (Fig. S**??**). Between one and three heating spots were made in a single cell. Diffraction patterns were collected at 42.7 keV using a Perkin Elmer (XRD1621) detector before and after heating but still at high pressure by performing 2D scanning maps over the heated area. The position and distance between the detector and the sample were calibrated using a CeO_2 standard. The diffraction patterns were analyzed using the DIOPTAS software by Prescher and Prakapenka (2015) for phase identification, pressure estimation, image integration, and background correction.

After the release of the pressure to ambient conditions, LH-DAC samples were recovered and further analyzed. Raman spectroscopy was performed

on the raw samples to assure no contamination of carbon from later sample preparation and, to detect diamonds in the experiments, as described in Drewitt et al. (2019). A HORIBA Jobin Yvon Confocal LabRAM HR 800 available at the University of Potsdam. Maps covering the entire area of the sample chamber were made using a grid of 2×2 µm^2 or 4×4 µm^2 steps, with 10 to 20 sec acquisition per spectrum. Spectra for diamond detection were acquired with a 532 nm laser and an 1800 gr/mm grating in 1300 to 1400 cm^{-1} spectral range. The processing of the Raman 2D maps was designed to search for the first-order diamond band at 1332 cm^{-1}. For each point of the maps, the diamond band integral was calculated using the spectral range between 1320 to 1340 cm^{-1}, and a baseline correction was applied by subtracting the background intensity obtained from 1360 to 1380 cm^{-1} spectral range (Fig 2A).

Samples were prepared for scanning transmission electron microscopy (STEM) analyses at the PISA facility at the Helmholtz-Zentrum Potsdam Deutsches GeoForschungsZentrum (GFZ), Potsdam (Germany) by drilling them out of the gaskets using the highly energetic Ga^+ ion beam of a Focused Ion Beam (FIB) FEI Helios G4 UC (Dual Beam). Discs of approximately 150-170 µm in diameter were glued onto an SEM holder and coated with amorphous carbon and then sectioned parallel to the compressional axis to access the laser-heated region. When the center of the heated region was revealed, a 2 µm thick Pt layer was deposited to protect the sample surface from the Ga^+ ion beam during the foil preparation. FIB lamellae were extracted and fixed on a copper grid and then thinned to a thickness of 3 µm. Samples were analyzed by energy dispersive X-ray (EDX) maps using an FEI

Quanta 3D (Dual Beam). Afterwards, several foils were thinned to electron transparency (∼100 nm thickness) and analyzed by STEM, EDX spectra mapping, electron diffraction (ED), and electron energy loss spectroscopy (EELS) using a Thermo Fisher Scientific Themis Z transmission electron microscope. The instrument is equipped with an aberration corrector at the probe side, a SuperX EDX 4 quadrant detector, and a Gatan Imaging Filter (GIF) Continuum 1065. The microscope was operated at 300 kV. All EDX maps were collected using a 50 pA electron beam and averaged multiple frame acquisition. The experimental conditions and run products of each experiment are reported in Table S**??**.

3. Results

The first set of the five multi-anvil experiments revealed the occurrence of melt at 25 GPa and between 1600 to 2000 K (Table 2). Despite modest temperatures, all runs performed were above the solidus and contained an assemblage of ferromagnesite [$(Mg_{0.88-0.95}Fe_{0.04-0.06})CO_3$], bridgmanite [$(Mg_{0.86-0.92}Fe_{0.10-0.13})SiO_3$], stishovite ($SiO_2$) and quenched melt (QM) (Fig.1, Table S**??**). Rhenium shards are observed in all capsules. In two experiments (#6 and #7, Table S**??**), ReO_2 and (Re,Fe,Mg)-oxide were found in the vicinity of the melt pockets, likely from an interaction between the rhenium capsules and the carbon-rich melt produced. Re–ReO_2 is a solid state metal-oxide buffer, and may therefore have influenced the oxygen fugacity in the multi-anvil experiments at around +5 log units relative to iron-wüstite (IW) (Rohrbach and Schmidt, 2011).

Quenched melt is identified in all MAP experiments by its dendritic tex-

Run n°	P (GPa)	Temp. (K)	Dur. (min)	Starting mat.	Run products
Multi-anvil experiments					
#4a [1]	25	2000	60	MG11:Sr	Bdg, Mgs, Sti, Fp, QM
#4b [1]	25	2000	60	MG11:La	Bdg, Mgs, Sti, Fp, QM
#5	25	1800	135	MG11:La	Bdg, Mgs, Sti, QM
#6	25	1900	135	MG11:La	Bdg, Mgs, Sti, QM, Re-Ox
#7	25	1800	135	MG11:Sr	Bdg, Mgs, Sti, QM, Re-Ox
#9	25	1600	120	MG11:La	Bdg, Mgs, Sti, QM, La-Si
LH-DAC experiments					
ON01	41	1750	23	MG11	Bdg, Mgs, Sti, Dia, Fp
ON02	41	1450	36	MG11	Bdg, Mgs, Sti, Dia, Fp
ON03	41	1600	26	MG11	Bdg, Mgs, St, Fp*
ON06	68	1850	33	MO13 + Pt	Ol, Bdg, Sti, Dia
ON07	68	2000	27	MO13 + Pt	Ol, Bdg, Sti, Dia
ON08	44	1900	30	MG11	Bdg, Sti, Dia, Fp*
ON11	40	2050	36	MO13 + Pt	Ol, Bdg, Dia, Fp, Mgs
ON13	40	2000	22	MO13 + Pt	Ol, Bdg, Dia, Fp*
ON19	51	1700	21	MG11	Bdg, Mgs, Sti, Dia
ON20	51	1400	14	MG11	Bdg, Mgs, Sti, Fp*
ON21	33	1650	14	MG13	Bdg, Mgs, Dia, Fp
ON22	33	1350	12	MG13	Bdg, Mgs, Dia, Fp
ON25	62	1650	13	MG11	Bdg, Mgs, Sti, Dia, Fp
ON26	62	1700	18	MG11	Bdg, Mgs, Sti, Fp*
ON27	62	1350	5	MG11	Bdg, Mgs, Sti, Dia, Fp
ON28	56	1400	11	MG11	Bdg, Mgs, Sti, Fp*
ON29	56	1900	8	MG11	Bdg, Mgs, Sti, Dia, Fp, Wus
ON31	66	1400	14	MG11	Bdg, Mgs, Sti, Dia, Fp*
ON32	66	1650	17	MG11	Bdg, Mgs, Sti, Dia
ON33	66	1500	16	MG11	Bdg, Mgs, Sti, Fp*
ON34	43	1300	14	$(Mg, Fe)SiO_3$ glass	Bdg, Sti, Fe-metal

Table 2: Compilation of observed phases from all analytical methods in multi-anvil and LH-DAC experiments presented in this work. [1] two capsules were placed inside a single experiment. Phases: Bdg - Bridgmanite, Sti - Stishovite, Mgs - Magnesite, Dia - Diamond, Fp - Ferropericlase; Fp* was not observed directly but assumed, Ol - Olivine, Wus - Wüstite, QM - Quenched melt, Re-Ox - Rhenium oxide, La-Si - Lanthanum-Silicate, Pt - Black platinium. Details of major element composition for multi-anvil experiment can be found in Table S**??** and analytical investigations used for each run of LH-DAC experiments are provided in Table S**??**.

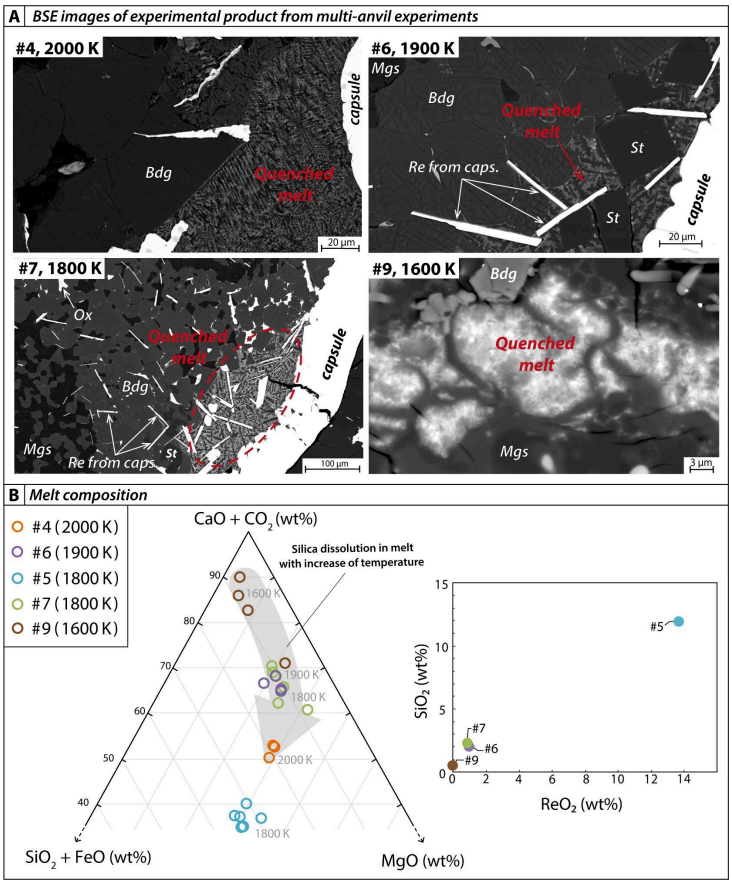

Figure 1: Results from the multi-anvil experiments. A) Back-scatter electron images of experimental products from multi-anvil quench experiments. Melt pockets (in red) are located in the hottest area of the capsules. Bdg: bridgmanite, Mgs: magnesite, St: stishovite, capsules are made of rhenium. B) Composition of melts from EPMA analyses.

ture (Fig.1A) and confirmed by the presence of the incompatible Sr and La dopants (Table S**??**). Therefore, these experiments indicate that the solidus line must be lower than the lowest temperature achieved in this study (#9, 1600 K at 25 GPa). Silicate mineral grains were found to be larger in the proximity of the melt pockets than elsewhere in the capsule (Fig.1A). This is particularly evident in the case of stishovite grains, indicating that stishovite growth is enhanced by melt. No bubbles were observed, suggesting that no CO_2-fluid was produced. The composition of the quenched melt evolves with increasing temperature (Fig.1B) from essentially silica-free and carbon-rich at 1600 K to 11 wt.% SiO_2 at 2000 K (Table S**??**). Run #5 is an exception to this trend, with an even higher enrichment of SiO_2, and ReO_2 reaching 13.7 wt.% (Fig. 1B). This systematic trend observed in the quenched melt composition (Fig.1B) indicates that a thorough chemical exchange between solids and melt was established in our multi-anvil experiments. The textures of the samples after the experiment revealed that significant temperature gradients were present and that the quenched melt is located at the hottest part of the capsules (center). The enrichment of La or Sr in the quenched melt further supports thorough chemical exchange that likely involved transport along T-gradients. Previous time series on the carbonate-peridotite system have shown that equilibrium was reached within ∼10 hours at 1500 °C and 6 GPa at an overall carbonate content of only 10% of the starting material (Brey et al., 2008). However, due to the high proportion of carbonate in our experiments chemical transport within the capsule is facilitated, as in the pure carbonate ($CaCO_3$–$MgCO_3$) system equilibrium was reached within 1 h 18 min at 1700 °C (Sieber et al., 2022). Representative major element

compositions obtained by EPMA are reported in Table S**??**.

The second set of experiments was performed using LH-DAC, including one reference LH-DAC experiment (ON34, see Table 2 and S**??**), containing only the synthetic silicate glass used in MG11 and MG13 without magnesite in order to investigate the phase assemblage that forms from the crystallization of the silicate glass in the absence of magnesite. Results obtained from the diffraction patterns of our LH-DAC experiments exhibited peaks corresponding to bridgmanite, stishovite, NaCl (pressure medium), and in some cases magnesite (Fig. S **??**). Bridgmanite was observed in all runs including the reference experiment that did not contain magnesite in the starting material (ON34, Fig. S **??**). Consequently, bridgmanite formed from our silicate starting material. In addition, no decarbonation products, i.e., diamond or CO_2, were identified with in situ XRD, mainly due to peaks overlapping in multi-phase systems, which complicates the analyses of run products analyses. Furthermore, the X-ray focus size, the small volume of material being probed, and the relatively low scattering power of carbon and oxygen create an extremely challenging environment to detect carbon-bearing phases, as also stated in previous studies (Drewitt et al., 2019; Mao and Boulard, 2013).

Fig. 2A1 shows a representative example of a processed 2D map obtained by Raman spectroscopy revealing the presence of diamond in run ON21 (33 GPa and 1650 K), which was later confirmed during FIB preparation Fig. S**??**. In contrast, no diamond peaks were detected in run ON22 (33 GPa and 1350 K) in the same Raman 2D map, but STEM analyses confirmed later the presence of nanometer-sized diamonds in this run (ON22,

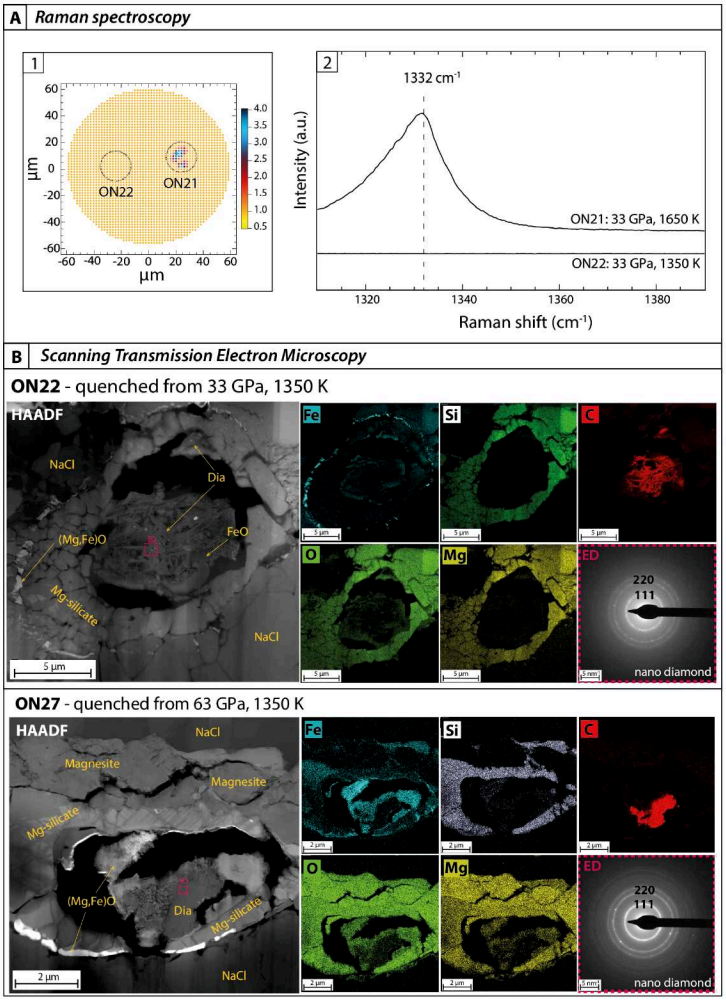

Figure 2: Results from ex situ analyses of recovered LH-DAC samples. A) (1) Example of Raman spectra illustrating the process of diamond detection, by investigating the presence of the first-order diamond peak at 1332 cm^{-1}, with (2) the examples of two experimental points (ON21 and ON22) confirming either the presence (ON21) or the absence (ON22) of diamond within the sensitivity of the equipment. B) HAADF-STEM images, EDX maps, and electron diffraction (ED) from nano-diamonds of selected recovered samples (ON22 and ON27) with red dashed rectangles on the HAADF images indicate the localization of the ED measurements. Reaction zones (hottest area) display in their center nano-sized diamond, that for ON22 was undetected by Raman spectroscopy. Around the nano-diamond center, the presence of Mg-silicate and a ring of ferropericlase delimit the reaction zone. The presence of wüstite (FeO) was found in a couple of experiments next to nano-diamond. The ON27 Raman 2D map is provided in supplementary material in Fig. S??, and close-up view of the nano-diamond area of ON22 and ON27 in Fig. S??

Fig. 2B). Therefore, STEM analyses have been shown to be the preferred analytical tool for identifying the presence of nanometer-sized diamonds. In contrast, Raman spectroscopy is more susceptible to being affected by non-perfect sample properties such as the unpolished sample surface, and the dark heated area, which reduces the penetration thickness and scattering efficiency of the Raman laser (see Table S**??**). Accordingly, unsuccessful STEM sample preparation by FIB milling directly caused an incapacity to confirm diamond presence for some runs, as well as expected reaction phases such as ferropericlase, that were undetectable by XRD. However, from our lowest temperature observation, it can be assumed that diamond formation happened under all conditions.

Textural and chemical features observed by STEM (Fig. 2B) are similar in all investigated experiments. The location of the laser-heated reaction center was easily identified as a round-shaped area, with a concentric distribution of phases (Fig. 2B). Within the center, a mixture of nanometer-sized diamonds, and ferropericlase, or wüstite (FeO), was observed. Crystal structures were confirmed using ED and EELS (Fig. 2B and Fig. S**??** for FeO in ON29). An iron-depleted amorphous silicate phase, interpreted as bridgmanite before quenching, surrounds the 'diamond-ferropericlase' center. The amorphization of the bridgmanite may have been caused by the Ga^+ beam during FIB milling (Marquardt and Marquardt, 2012). A ring of ferropericlase encloses and marks the border of the heated area. The surrounding volume consists of NaCl and unheated starting materials, which explains the presence of magnesite peaks in the diffraction patterns after heating since the XRD probed the entire thickness of the sample. The ferropericlase ring

likely results from chemical migration during laser heating, which is a distinct effect of a radial temperature gradient in LH-DAC experiments. The quench textures of the reaction zones are very heterogeneous, with different phases that crystallize. If a melt was present during the quench, we could have identified a homogeneous region (e.g. a melt pool) in the center of the heated area. Solid state experiments (Sinmyo and Hirose, 2010) as well as partial melting experiments (Baron et al., 2022) describe similar quenched textures emphasizing that the described texture is not sufficient to distinguish between sub-solidus and supra-solidus conditions. Further, the XRD settings did not allow the recording of diffuse signals from a weakly scattering carbonate melt. If partial melting occurred the melt may have undergone immediate redox freezing to diamond and ferropericlase, both occurring within the reaction zone (Fig. 2B).

Our starting material was placed within two layers of NaCl acting as a pressure-transmitting medium, an insulator from the diamond anvil as well as to limit element segregation during laser heating. No reaction products such as Na-carbonates were found, neither by XRD nor during STEM analyses, that could have affected the system compositions. This is also supported by the sharp contact observed between NaCl and other phases, in Fig. 2B and Fig. S**??**.

In the reference experiment (ON34), the STEM investigation revealed that heating of the starting glass results in the crystallization of a phase mixture of bridgmanite, stishovite, and metallic iron. Stishovite was identified from pure SiO_2 regions in EDX maps and confirmed by ED (Fig. S**??**). Metallic iron was identified in elemental maps as oxygen-depleted versus iron-

rich regions. Chemical analyses revealed high iron concentration and an oxygen K-edge peak too low to be an iron-oxide. Previous studies have reported the occurrence of metallic iron grains in lower mantle phase assemblages due to the Fe disproportionation reaction (Dorfman et al., 2021; Auzende et al., 2011; Frost et al., 2004). Additionally, the presence of metallic iron suggests that the redox conditions are at $\Delta \log f\mathrm{O}_2$ around 0 to -1.5 relative to the IW buffer (Rohrbach and Schmidt, 2011). Although observed in ON34, metallic iron was not found in any run loaded with magnesite indicating that it reacted completely to form oxides (Fig. S**??**).

Here, we assume that stishovite is produced by exsolution as a result of low Fe solubility in bridgmanite that cannot accommodate all Fe available and that ferropericlase is a reaction product of the decarbonation reaction of magnesite to diamond. However, no diffraction peaks of ferropericlase and/or metallic iron could be identified, even in ON34. Therefore, ferropericlase is assumed to be present, although not observed (Table 2), in experiments in which stishovite or diamond was observed. However, given the Fe-content of the bridgmanite-glass, the enhanced solubility of Fe in bridgmanite for pressures exceeding ∼20 GPa (Dorfman et al., 2021, 2013) should lead to the incorporation of all provided Fe in bridgmanite. In contrast, we report crystallization to a mixture of metallic Fe, stishovite, and bridgmanite up to 43 GPa at 1300 K (run ON34). It could also be possible that a slight non-stoichiometric excess of SiO_2 in our starting material could lead to the exsolution of stishovite during the crystallization of the glass. Additionally, iron could also dissolve in the melt at high pressure and temperature and eventually quench to nano-crystalline ferropericlase or wüstite in the quenched

silicate melt, which was observed by SEM. This highlights the need to investigate further the Fe-solubility in bridgmanite as a function of temperature and oxygen fugacity. Our results do not provide conclusive information in this regard.

Four pressure-temperature points (ON06, ON07, ON11, and ON13) were investigated with the MO11 starting material containing Pt (as a laser coupler). Despite the difference in the starting composition, XRD revealed the same phase assemblage as in other runs (Table S**??**). However, none of these samples were recovered successfully for STEM investigation, and only Raman spectroscopy identified the presence of diamonds in the 4 experiments. Therefore, no additional data could be collected to evaluate the potential effects of (1) the change of starting composition in the reaction and (2) Pt on the Fe contained in the sample

Most STEM foils show void areas that are associated with cracks formed during decompression, manipulation, and thinning during FIB milling. Most damages were caused by the beam used during EDX mapping at the FIB-SEM and failed attempts of field emission gun electron microprobe (FEG-EMP) mapping, performed before STEM analyses. All experimental conditions, run products, and analytical investigations used for each run are provided in Table 2 and in detail in Table S**??**.

4. Discussion

4.1. The fate of deeply subducted magnesite

Our results provide new insights into the stability field of magnesite in the presence of Fe-bearing lower mantle assemblages (Fig. 3). Our experiments

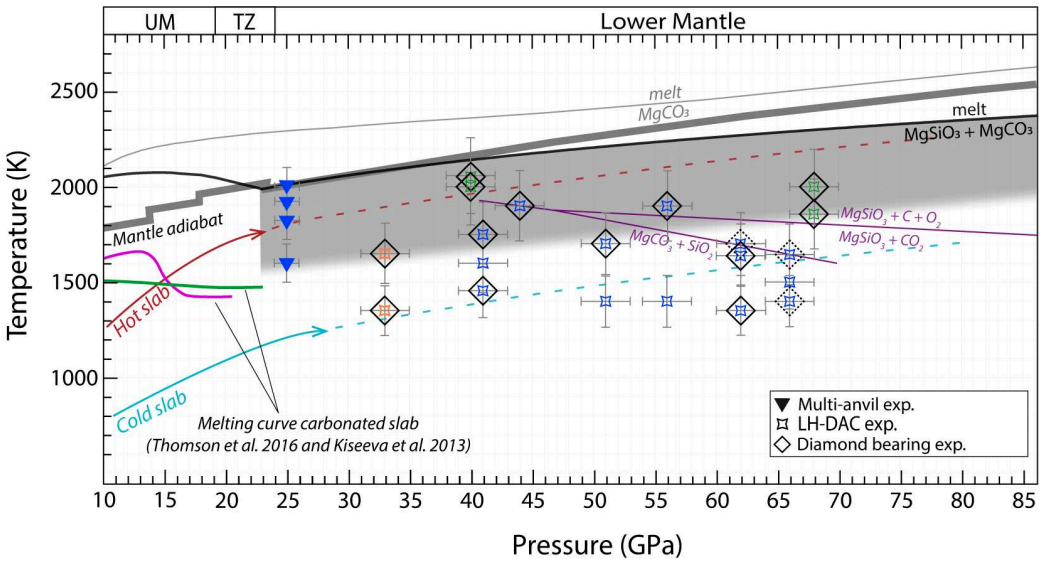

Figure 3: Pressure-temperature diagram of carbonates stability within subducted oceanic crust through Earth's mantle. Top grey line is the melting curve of $MgCO_3$ constrained by Solopova et al. (2015) and black line is the melting curve of $MgCO_3$ + $MgSiO_3$ according to Thomson et al. (2014). Purple lines indicate decarbonation reaction of $MgCO_3$ + SiO_2 from Drewitt et al. (2019). The bold grey line is the mantle adiabat after Katsura et al. (2010). Typical slab geotherms (hot slab in red and very cold slab in sky blue) are modified from Maeda et al. (2017). The colors of symbols refer to the starting composition used in our experiments: blue = MG11; orange = MG13 and green = MO11. Symbols correspond to the experimental technique used, triangle for multi-anvil and stars for LH-DAC experiments. Grey-shaded zone indicates the area where melting is expected in our system. Symbols encased in a diamond shape indicate the presence of diamonds that were confirmed by Raman spectroscopy and/or STEM, the dashed diamond shape was only confirmed by EDX during FIB milling. The absence of the diamond shape indicates experiments in which diamonds were not detected during Raman measurements and could not be investigated by STEM because of preparation failure during FIB milling. UM: Upper mantle and TZ: Transition Zone.

reveal the breakdown of magnesite by (1) the presence of a carbonate-melt in multi-anvil experiments by melting at 25 GPa and 1600–2000 K (downward triangle in Fig.3), and (2) the presence of diamond in LH-DAC experiments via a 'decarbonation reaction' at 33–75 GPa and 1300–2000 K (diamond shape around star symbols in Fig.3). These results notably differ from previous investigations utilizing simplified iron-free systems (Maeda et al., 2017; Kakizawa et al., 2015; Litasov and Shatskiy, 2019), indicating that the presence of iron plays a major role in magnesite stability, as previously suggested by experimental investigations (Dorfman et al., 2018).

The previously determined melting curve of the iron-free $MgCO_3 + MgSiO_3$ system at lower mantle depths (constrained by LH-DAC experiments) indicates eutectic melting at 25 GPa and ∼2000 K (Thomson et al., 2014). In contrast, our results on the Fe-containing–plus a minor amount of either Sr or La–system reveal that melting occurs at temperatures 400 K lower (1600 K at 25 GPa). The lower melting temperature may be explained by the addition of Fe, which should lower the temperature of the eutectic as found for other Fe-Mg silicate systems (Agee et al., 1995). Generally, the addition of components that do not induce immiscibility in the melt phase should lead to lowering of the melting temperature. This is exemplified in carbonated-MORB systems such as in Kiseeva et al. (2013) and Thomson et al. (2016b), with compositions containing respectively 3.54 to 3.78 wt% and 2.58 wt% of $Na_2O + K_2O$ in total in their starting material, an even lower melting temperature is obtained reaching ∼1400 K, if extrapolated up to 25 GPa. Our data, coupled with published data sets, support that at more oxidizing conditions, around the Re-ReO_2 buffer, melting may be an important mech-

458 anism for the elimination and recycling of carbonates from the subducted
459 oceanic lithosphere, along all subduction geotherms except for the very cold
460 ones (Drewitt et al., 2019; Maeda et al., 2017).

461 Experimental investigations have shown that if carbonate melts infiltrate
462 the reduced ambient mantle at depths ≥250 km, the melt will become un-
463 stable and will be reduced to diamond via redox freezing (Rohrbach and
464 Schmidt, 2011). The presence of Re/ReO_2 in our multi-anvil experiments
465 suggests that the experimental redox conditions might have been too oxi-
466 dized (around IW +4 to +5) (Rohrbach and Schmidt, 2011) when compared
467 to expected deep mantle conditions (around IW to IW -1.5) (Frost and Mc-
468 Cammon, 2008), thus may have prevented diamond nucleation. However,
469 diamond formation was observed in our LH-DAC experiments at tempera-
470 tures as low as, and even lower than, the coldest subduction geotherm at
471 33 GPa (1350 K) and at 62 GPa (1350 K), respectively (Fig. 3). The ex-
472 perimental conditions in which diamonds are observed differ noticeably from
473 the ones reported in Drewitt et al. (2019) (purple lines in Fig. 3). These dif-
474 ferences can result from the differences between starting bulk compositions,
475 highlighting the necessity to couple several analytical techniques such as in
476 situ or ex situ XRD, Raman and/or STEM in multi-phases run products in
477 LH-DAC experiments (see Results).

478 The breakdown of magnesite into diamond in LH-DAC experiments im-
479 plies the presence of a reducing agent. Previous studies have shown that
480 metallic iron is a relevant reducing agent for magnesite (Dorfman et al.,
481 2018; Martirosyan et al., 2019; Zhu et al., 2019), but these studies do not
482 account for the presence of silicates. The results of our magnesite-free refer-

ence experiments (ON34, see methods and results) show that metallic iron is produced during the crystallization of our starting silicate glass. Neither metallic iron nor Fe-carbides were observed to co-exist with diamond, indicating that the metallic iron may have formed as an intermediate phase and then was completely consumed by reacting with $MgCO_3$ to form diamond via redox freezing (see Eq. 1). Whereas the remaining Fe^{2+} is partitioned into ferropericlase and/or wüstite and the Fe^{3+} into bridgmanite.

We do not have a similar experiment to ON34, with only olivine as the starting material. However, previous studies have investigated lower mantle assemblages using olivine with a similar composition to the one of this study (Auzende et al., 2008). They reported a mixture of bridgmanite, ferropericlase, and iron metal as run products attributed to disproportionation in bridgmanite (Frost et al., 2004). With the increase in pressure, the iron's solubility in bridgmanite increases too, and can reach up to ∼75 mol% at deep lower mantle conditions (∼90 GPa) (Dorfman et al., 2013). This indicates, that at higher pressure, the olivine starting material does not crystallize in a mixture of phases but only as single-phase bridgmanite, since it can accommodate the iron completely. However, in the highest pressure explored in this study (e.g. ON07 at 68 GPa and ON31/32/33 at 66 GPa), stishovite was observed in the in situ XRD, meaning that it is likely that the iron was not fully incorporated in the bridgmanite and that a mixture of bridgmanite + stishovite + ferropericlase and probably metallic iron were produced. While, without direct observations, we cannot fully rule out the presence of metallic iron, we consider that some might have formed in these experiments.

The temperatures of diamond formation reported here are lower than the

melting temperatures reported from our multi-anvil experiments, whereas no satisfactory evidence of melting was observed in our LH-DAC experiments such as diffuse scattering during heating in our XRD spectra. Nonetheless, we expect that the shape of our iron-bearing melting curve will be parallel to the iron-free curve by Thomson et al. (2014), adjusted to considerably lower temperatures. The newly derived iron-bearing melting area (grey area in Fig. 3) indicates that melting may occur at similar temperatures (but higher pressures) at which diamond crystallization is observed. This superimposition highlights a possible dynamic relationship between diamond crystallization and melting. Indeed, super-deep diamonds originating from depths from $\geq$250 km to the transition zone appear to have crystallized from low-degrees of partial melting of subducted carbonate-rich oceanic crust, as indicated by the elevated trace elements content within super-deep diamond mineral inclusions (Walter et al., 2008; Bulanova et al., 2010; Thomson et al., 2016a; Walter et al., 2022). In addition, oxygen (^{18}O) isotopic compositions from mineral inclusions in super-deep diamonds, coupled with carbon (^{13}C) and nitrogen (^{15}N) isotopic compositions from the diamond hosts, reveal that the carbon source for diamond formation is depth-dependent. Whereas sub-lithospheric diamonds that crystallize at depths $\leq$700 km (up to the shallow lower mantle) indicate a source from recycled oceanic crust, diamonds formed at depths $\geq$700 km lack evidence of such a source, supporting the barrier for carbon subduction at the top of the lower mantle (Regier et al., 2020).

Our study is not sufficient to respond on whether or not diamond formation necessarily involves redox freezing of a carbon-rich melt or happens as a sub-solidus reaction but rather serve to look for fundamental chemical inter-

actions in multiphase systems in which carbonates and lower mantle silicate interact. Therefore, further experiments are needed to localize the solidus in the investigated system. Nevertheless, the presence of diamond in our data clearly demonstrates that magnesite is not stable when in contact with (Mg, Fe)-silicates at depths reflecting the shallow lower mantle (25 to 60 GPa) and suggests that magnesite will unlikely be preserved throughout the lower mantle, even if transported in the coldest slab. Accordingly, the recycling of magnesite within the shallow lower mantle ($\leq$40 GPa) inhibits the transport of carbonates to Earth's deeper interior.

4.2. Implications for the genesis of super-deep diamonds

One persisting uncertainty is whether or not subducted carbonates will survive within slabs to depths of at least 660 km without being reduced to diamonds at shallower depths since Fe-metal is already stable at 250 km (Frost et al., 2004). The recent study of Martirosyan et al. (2022) assessed the complexities of carbonate + silicates + Fe redox interactions and evaluated their reaction kinetics at upper-mantle and hot subduction geotherm conditions (6 GPa and $\sim$1400 K). Their results indicate that the presence of silicates in an anhydrous and melt-free environment will slow down the redox reaction due to the barrier that silicates constitute on Fe and O diffusion. In such a scenario, carbonates may persist and reach the lower mantle and provide the carbon source for super-deep diamonds. Seismic imaging indicates that slabs can stagnate at the shallow lower mantle due to an increase of mantle viscosity (Fukao and Obayashi, 2013; Marquardt and Miyagi, 2015). This stagnation may promote an environment where carbonated slabs accumulate, increasing the amount of oxidized reactant over time to reduce and

form super-deep diamonds, even in the coldest subduction as shown by our data. As a result, a diamond production region (Zhu et al., 2019) is expected at the transition zone/lower mantle boundary. The rate of subduction will have a great influence on the supply of oxidized carbon necessary to produce diamonds over geological time since the concentration of carbonates present in slabs is limited to ∼0.3 wt.% (Dasgupta and Hirschmann, 2010). The influx of oxidized carbon in the form of solid carbonates or carbonate-melt in this mantle region is expected to buffer the fugacity locally (Stagno et al., 2019, 2011) by the consumption of metallic iron nearby, as seen in our LH-DAC experiments. A metal-free mantle region may result if the supply of oxidized phases surpasses the redox metallic iron capacity locally. Such localized fO_2 disparities are revealed from carbonate inclusions in diamonds (Brenker et al., 2007; Kaminsky, 2012; Bulanova et al., 2010), reflecting a higher oxidation state within the diamond production region, around IW +2 to +3 (at ∼25 GPa) where magnesite and diamond co-exist (Stagno et al., 2011).

The re-mobilization of such diamonds by mantle upwelling to lower depths ≤250 km (where the ambient mantle ceases to be metal saturated) will form carbonate-melt via the redox melting, the inverse process of redox freezing (Rohrbach and Schmidt, 2011). Those melts may then transport carbon back to the surface in a rising mantle plume, such as within ocean-island basalts (OIB) or carbonatites (Hammouda and Keshav, 2015; McCammon et al., 2020; Dasgupta and Hirschmann, 2010).

5. Conclusion

We conducted a multi-experimental and analytical study using multi-anvil apparatus and laser-heated diamond anvil cells to investigate the reaction between magnesite and iron-bearing bridgmanite. This reaction is used as an experimental proxy to investigate the interactions of carbonate minerals contained within the oceanic crust subducting into the lower mantle. Our data demonstrate that magnesite is not stable in the Fe-bearing system at cold slab temperatures (1350 K) and shallow lower mantle conditions (33 GPa). Magnesite is thus unlikely to carry oxidized carbon deeper into the reduced lower mantle to depths greater than 700 km. Carbon will instead be present in its immobile and reduced form, diamond, and stored over long timescales in the deep mantle where it could be re-mobilized by mantle upwelling. Furthermore, we can speculate that the reduction of carbonate minerals contained in stagnating slabs will consume the metallic iron and produce a locally oxidized mantle, creating regions where oxidized and reduced carbon phases may co-exist.

Acknowledgments

Financial support for this study was provided by the German Science Foundation (DFG) through the CarboPaT research unit FOR2125 (WI 2000/8-2, AP 262/1-2) and by the Federal Ministry of Education and Research of Germany (Project No. 05K19IP2). We acknowledge Deutsches Elektronen-Synchrotron DESY (Hamburg, Germany), a member of the Helmholtz Association HGF, for the provision of experimental facilities. Parts of this research were carried out at the ECB beamline (P02.2) and we would like to thank

Konstantin Glazyrin and Rachel J. Husband for their assistance. Beamtime was allocated for proposal(s) I-20190107, I-20190784, and I-20200105. Funding from the European Regional Development Fund and the State of Brandenburg for the Themis TEM (part of the "Potsdam Imaging and Spectral Analysis Facility" (PISA)), is gratefully acknowledged. We greatly thank T. Katsura, D. Frost, S. Shcheka, and the Bayerisches Geoinstitut for welcoming us to perform our multi-anvil press experiments. LL sincerely thanks Cody L. Colleps for support with the English writing and correction, Christine Fischer for support with sample preparation, Christina Günter for assistance during EPMA analyses, and Christoph Möller for help with the Raman 2D maps processing. IB acknowledges funding from DFG projects BL1690/1-1 and BL1690/1-2.

Appendix A. Supplementary materials

Supplementary materials can be found in the document "Supplementary information".

References

Agee, C., Li, J., Shannon, M., Circone, S., 1995. Pressure-temperature phase diagram for the Allende meteorite. Journal of Geophysical Research: Solid Earth 100, 17725–17740.

Akahama, Y., Kawamura, H., 2006. Pressure calibration of diamond anvil Raman gauge to 310 GPa. Journal of Applied Physics 100, 043516. doi:10.1063/1.2335683.

627 Auzende, A.L., Badro, J., Ryerson, F.J., Weber, P.K., Fallon, S.J., Addad,
628 A., Siebert, J., Fiquet, G., 2008. Element partitioning between magne-
629 sium silicate perovskite and ferropericlase: New insights into bulk lower-
630 mantle geochemistry. Earth and Planetary Science Letters 269, 164–174.
631 doi:10.1016/j.epsl.2008.02.001.

632 Auzende, A.L., Gillot, J., Coquet, A., Hennet, L., Ona-Nguema, G., Bonnin,
633 D., Esteve, I., Roskosz, M., Fiquet, G., 2011. Synthesis of amorphous
634 MgO-rich peridotitic starting material for laser-heated diamond anvil cell
635 experiments – application to iron partitioning in the mantle. High Pressure
636 Research 31, 199–213. doi:10.1080/08957959.2011.556631.

637 Baron, M.A., Fiquet, G., Morard, G., Miozzi, F., Esteve, I., Doisneau, B.,
638 Pakhomova, A.S., Ricard, Y., Guyot, F., 2022. Melting of basaltic litholo-
639 gies in the earth's lower mantle. Physics of the Earth and Planetary Inte-
640 riors 333, 106938. doi:10.1016/j.pepi.2022.106938.

641 Biellmann, C., Gillet, P., Guyot, F., Peyronneau, J., Reynard, B., 1993.
642 Experimental evidence for carbonate stability in the Earth's lower man-
643 tle. Earth and Planetary Science Letters 118, 31–41. doi:10.1016/0012-
644 821x(93)90157-5.

645 Binck, J., Bayarjargal, L., Lobanov, S.S., Morgenroth, W., Luchitskaia,
646 R., Pickard, C.J., Milman, V., Refson, K., Jochym, D.B., Byrne,
647 P., Winkler, B., 2020. Phase stabilities of $MgCO_3$ and $MgCO_3$-II
648 studied by Raman spectroscopy, X-ray diffraction, and density func-
649 tional theory calculations. Physical Review Materials 4, 055001.
650 doi:10.1103/PhysRevMaterials.4.055001.

651 Brenker, F.E., Vollmer, C., Vincze, L., Vekemans, B., Szymanski, A.,
652 Janssens, K., Szaloki, I., Nasdala, L., Joswig, W., Kaminsky, F.,
653 2007. Carbonates from the lower part of transition zone or even
654 the lower mantle. Earth and Planetary Science Letters 260, 1–9.
655 doi:10.1016/j.epsl.2007.02.038.

656 Brey, G.P., Bulatov, V.K., Girnis, A.V., Lahaye, Y., 2008. Experimental
657 melting of carbonated peridotite at 6–10 GPa. Journal of Petrology 49,
658 797–821. doi:10.1093/petrology/egn002.

659 Bulanova, G.P., Walter, M.J., Smith, C.B., Kohn, S.C., Armstrong, L.S.,
660 Blundy, J., Gobbo, L., 2010. Mineral inclusions in sublithospheric dia-
661 monds from Collier 4 kimberlite pipe, Juina, Brazil: subducted protoliths,
662 carbonated melts and primary kimberlite magmatism. Contributions to
663 Mineralogy and Petrology 160, 489–510. doi:10.1007/s00410-010-0490-6.

664 Connolly, J.A., 2005. Computation of phase equilibria by linear program-
665 ming: a tool for geodynamic modeling and its application to subduction
666 zone decarbonation. Earth and Planetary Science Letters 236, 524–541.
667 doi:10.1016/j.epsl.2005.04.033.

668 Dasgupta, R., Hirschmann, M.M., 2006. Melting in the Earth's deep
669 upper mantle caused by carbon dioxide. Nature 440, 659–662.
670 doi:10.1038/nature04612.

671 Dasgupta, R., Hirschmann, M.M., 2010. The deep carbon cycle and melt-
672 ing in Earth's interior. Earth and Planetary Science Letters 298, 1–13.
673 doi:10.1016/j.epsl.2010.06.039.

Dorfman, S.M., Badro, J., Nabiei, F., Prakapenka, V.B., Cantoni, M., Gillet, P., 2018. Carbonate stability in the reduced lower mantle. Earth and Planetary Science Letters 489, 84–91. doi:10.1016/j.epsl.2018.02.035.

Dorfman, S.M., Meng, Y., Prakapenka, V.B., Duffy, T.S., 2013. Effects of Fe-enrichment on the equation of state and stability of (Mg, Fe)SiO_3 perovskite. Earth and Planetary Science Letters 361, 249–257. doi:10.1016/j.epsl.2012.10.033.

Dorfman, S.M., Nabiei, F., Boukaré, C.E., Prakapenka, V.B., Cantoni, M., Badro, J., Gillet, P., 2021. Composition and Pressure Effects on Partitioning of Ferrous Iron in Iron-Rich Lower Mantle Heterogeneities. Minerals 11, 512. doi:10.3390/min11050512.

Drewitt, J.W., Walter, M.J., Zhang, H., McMahon, S.C., Edwards, D., Heinen, B.J., Lord, O.T., Anzellini, S., Kleppe, A.K., 2019. The fate of carbonate in oceanic crust subducted into earth's lower mantle. Earth and Planetary Science Letters 511, 213–222. doi:10.1016/j.epsl.2019.01.041.

Fei, Y., Ricolleau, A., Frank, M., Mibe, K., Shen, G., Prakapenka, V., 2007. Toward an internally consistent pressure scale. Proceedings of the National Academy of Sciences 104, 9182–9186. doi:10.1073/pnas.0609013104.

Fiquet, G., Auzende, A., Siebert, J., Corgne, A., Bureau, H., Ozawa, H., Garbarino, G., 2010. Melting of peridotite to 140 gigapascals. Science 329, 1516–1518. doi:10.1126/science.1192448.

Frost, D.J., Liebske, C., Langenhorst, F., McCammon, C.A., Trønnes, R.G., Rubie, D.C., 2004. Experimental evidence for the existence of

697 iron-rich metal in the Earth's lower mantle. Nature 428, 409–412.
698 doi:10.1038/nature02413.

699 Frost, D.J., McCammon, C.A., 2008. The redox state of
700 Earth's mantle. Annu. Rev. Earth Planet. Sci. 36, 389–420.
701 doi:10.1146/annurev.earth.36.031207.124322.

702 Fukao, Y., Obayashi, M., 2013. Subducted slabs stagnant above, penetrating
703 through, and trapped below the 660 km discontinuity. Journal of Geophys-
704 ical Research: Solid Earth 118, 5920–5938. doi:10.1002/2013JB010466.

705 Ghosh, S., Ohtani, E., Litasov, K.D., Terasaki, H., 2009. Solidus of car-
706 bonated peridotite from 10 to 20 GPa and origin of magnesiocarbon-
707 atite melt in the Earth's deep mantle. Chemical Geology 262, 17–28.
708 doi:10.1016/j.chemgeo.2008.12.030.

709 Gorman, P.J., Kerrick, D., Connolly, J., 2006. Modeling open system meta-
710 morphic decarbonation of subducting slabs. Geochemistry, Geophysics,
711 Geosystems 7. doi:10.1029/2005GC001125.

712 Hammouda, T., Keshav, S., 2015. Melting in the mantle in
713 the presence of carbon: Review of experiments and discussion
714 on the origin of carbonatites. Chemical Geology 418, 171–188.
715 doi:10.1016/j.chemgeo.2015.05.018.

716 Hanfland, M., Syassen, K., Fahy, S., Louie, S.G., Cohen, M.L., 1986. The
717 first-order Raman mode of diamond under pressure. Physica B+ C 139,
718 516–519. doi:10.1016/0378-4363(86)90636-4.

719 Hennet, L., Thiaudiere, D., Gailhanou, M., Landron, C., Coutures, J.P.,
720 Price, D.L., 2002. Fast x-ray scattering measurements on molten alumina
721 using a 120 curved position sensitive detector. Review of scientific instru-
722 ments 73, 124–129. doi:10.1063/1.1426228.

723 Isshiki, M., Irifune, T., Hirose, K., Ono, S., Ohishi, Y., Watanuki, T.,
724 Nishibori, E., Takata, M., Sakata, M., 2004. Stability of magnesite
725 and its high-pressure form in the lowermost mantle. Nature 427, 60–63.
726 doi:10.1038/nature02181.

727 Kakizawa, S., Inoue, T., Suenami, H., Kikegawa, T., 2015. Decarbonation
728 and melting in $MgCO_3$–SiO_2 system at high temperature and high pres-
729 sure. Journal of Mineralogical and Petrological Sciences 110, 179–188.
730 doi:10.2465/jmps.150124.

731 Kaminsky, F., 2012. Mineralogy of the lower mantle: A review of 'super-
732 deep' mineral inclusions in diamond. Earth-Science Reviews 110, 127–147.
733 doi:10.1016/j.earscirev.2011.10.005.

734 Kaminsky, F.V., Ryabchikov, I.D., Wirth, R., 2016. A primary natrocar-
735 bonatitic association in the Deep Earth. Mineralogy and Petrology 110,
736 387–398. doi:10.1007/s00710-015-0368-4.

737 Kantor, I., Prakapenka, V., Kantor, A., Dera, P., Kurnosov, A., Sinogeikin,
738 S., Dubrovinskaia, N., Dubrovinsky, L., 2012. BX90: A new diamond
739 anvil cell design for X-ray diffraction and optical measurements. Review
740 of Scientific Instruments 83, 125102. doi:10.1063/1.4768541.

741 Katsura, T., Yoneda, A., Yamazaki, D., Yoshino, T., Ito, E., 2010. Adiabatic
742 temperature profile in the mantle. Physics of the Earth and Planetary
743 Interiors 183, 212–218. doi:10.1016/j.pepi.2010.07.001.

744 Kelemen, P.B., Manning, C.E., 2015. Reevaluating carbon fluxes in subduc-
745 tion zones, what goes down, mostly comes up. Proceedings of the National
746 Academy of Sciences 112, E3997–E4006. doi:10.1073/pnas.1507889112.

747 Keppler, H., Frost, D.J., 2005. Introduction to minerals under extreme con-
748 ditions, in: Mineral behaviour at extreme conditions. Mineralogical society
749 of Great Britain and Ireland, pp. 1–30. doi:10.1180/emu-notes.7.1.

750 Kerrick, D., Connolly, J., 2001. Metamorphic devolatilization of sub-
751 ducted oceanic metabasalts: implications for seismicity, arc magmatism
752 and volatile recycling. Earth and Planetary Science Letters 189, 19–29.
753 doi:10.1016/S0012-821X(01)00347-8.

754 Kiseeva, E.S., Litasov, K.D., Yaxley, G.M., Ohtani, E., Kamenetsky, V.S.,
755 2013. Melting and phase relations of carbonated eclogite at 9–21 GPa
756 and the petrogenesis of alkali-rich melts in the deep mantle. Journal of
757 Petrology 54, 1555–1583. doi:10.1093/petrology/egt023.

758 Konôpková, Z., Morgenroth, W., Husband, R., Giordano, N., Pakho-
759 mova, A., Gutowski, O., Wendt, M., Glazyrin, K., Ehnes, A., Delitz,
760 J.T., et al., 2021. Laser heating system at the Extreme Conditions
761 Beamline, P02.2, PETRA III. Journal of Synchrotron Radiation 28.
762 doi:10.1107/S1600577521009231.

763 Koziol, A.M., Newton, R.C., 1995. Experimental determination of the reac-
764 tions magnesite + quartz = enstatite + CO_2 and magnesite = periclase
765 + CO_2, and enthalpies of formation of enstatite and magnesite. American
766 Mineralogist 80, 1252–1260. doi:10.2138/am-1995-11-1215.

767 Liermann, H.P., Konôpková, Z., Morgenroth, W., Glazyrin, K., Bednarčik,
768 J., McBride, E., Petitgirard, S., Delitz, J., Wendt, M., Bican, Y., et al.,
769 2015. The extreme conditions beamline P02. 2 and the extreme conditions
770 science infrastructure at PETRA III. Journal of synchrotron radiation 22,
771 908–924. doi:10.1107/S1600577515005937.

772 Litasov, K., Shatskiy, A., 2019. $MgCO_3$ + SiO_2 reaction at pressures up to 32
773 GPa studied using in-situ x-ray diffraction and synchrotron radiation. Geo-
774 chemistry International 57, 1024–1033. doi:10.1134/S0016702919090064.

775 Litasov, K.D., Ohtani, E., 2009. Solidus and phase relations of carbonated
776 peridotite in the system CaO–Al_2O_3–MgO–SiO_2–Na_2O–CO_2 to the lower
777 mantle depths. Physics of the Earth and Planetary Interiors 177, 46–58.
778 doi:10.1016/j.pepi.2009.07.008.

779 Luth, R.W., 2001. Experimental determination of the reaction aragonite +
780 magnesite = dolomite at 5 to 9 GPa. Contributions to Mineralogy and
781 Petrology 141, 222–232. doi:10.1007/s004100100238.

782 Lv, M., Dorfman, S.M., Badro, J., Borensztajn, S., Greenberg, E.,
783 Prakapenka, V.B., 2021. Reversal of carbonate-silicate cation exchange
784 in cold slabs in earth's lower mantle. Nature Communications 12.
785 doi:10.1038/s41467-021-21761-9.

786 Maeda, F., Ohtani, E., Kamada, S., Sakamaki, T., Hirao, N., Ohishi, Y.,
787 2017. Diamond formation in the deep lower mantle: a high-pressure reac-
788 tion of $MgCO_3$ and SiO_2. Scientific reports 7, 1–7. doi:10.1038/srep40602.

789 Mao, W.L., Boulard, E., 2013. Nanoprobes for deep carbon. Reviews in
790 Mineralogy and Geochemistry 75, 423–448. doi:10.2138/rmg.2013.75.13.

791 Marquardt, H., Marquardt, K., 2012. Focused ion beam preparation
792 and characterization of single-crystal samples for high-pressure experi-
793 ments in the diamond-anvil cell. American Mineralogist 97, 299–304.
794 doi:10.2138/am.2012.3911.

795 Marquardt, H., Miyagi, L., 2015. Slab stagnation in the shallow lower mantle
796 linked to an increase in mantle viscosity. Nature Geoscience 8, 311–314.
797 doi:10.1038/ngeo2393.

798 Martirosyan, N., Shatskiy, A., Litasov, K., Sharygin, I., Yoshino, T.,
799 2022. Interaction of carbonates with peridotite containing iron metal:
800 Implications for carbon speciation in the upper mantle. Lithos ,
801 106817doi:10.1016/j.lithos.2022.106817.

802 Martirosyan, N.S., Litasov, K.D., Lobanov, S.S., Goncharov, A.F., Shatskiy,
803 A., Ohfuji, H., Prakapenka, V., 2019. The Mg-carbonate–Fe interac-
804 tion: Implication for the fate of subducted carbonates and formation
805 of diamond in the lower mantle. Geoscience Frontiers 10, 1449–1458.
806 doi:10.1016/j.gsf.2018.10.003.

807 McCammon, C., Bureau, H., Cleaves, J.H., Cottrell, E., Dorfman, S.M.,
808 Kellogg, L.H., Li, J., Mikhail, S., Moussallam, Y., Sanloup, C., et al.,

2020. Deep Earth carbon reactions through time and space. American Mineralogist: Journal of Earth and Planetary Materials 105, 22–27. doi:10.2138/am-2020-6888CCBY.

Molina, J.F., Poli, S., 2000. Carbonate stability and fluid composition in subducted oceanic crust: an experimental study on H_2O–CO_2-bearing basalts. Earth and Planetary Science Letters 176, 295–310. doi:10.1016/S0012-821X(00)00021-2.

O'Neill, H.S., Berry, A.J., Mallmann, G., 2018. The oxidation state of iron in mid-ocean ridge basaltic (morb) glasses: Implications for their petrogenesis and oxygen fugacities. Earth and Planetary Science Letters 504, 152–162. doi:10.1016/j.epsl.2018.10.002.

Plank, T., Manning, C.E., 2019. Subducting carbon. Nature 574, 343–352. doi:10.1038/s41586-019-1643-z.

Prescher, C., Prakapenka, V.B., 2015. DIOPTAS: a program for reduction of two-dimensional X-ray diffraction data and data exploration. High Pressure Research 35, 223–230. doi:10.1080/08957959.2015.1059835.

Regier, M., Pearson, D., Stachel, T., Luth, R., Stern, R., Harris, J., 2020. The lithospheric-to-lower-mantle carbon cycle recorded in superdeep diamonds. Nature 585, 234–238. doi:10.1038/s41586-020-2676-z.

Rohrbach, A., Ballhaus, C., Golla-Schindler, U., Ulmer, P., Kamenetsky, V.S., Kuzmin, D.V., 2007. Metal saturation in the upper mantle. Nature 449, 456–458. doi:10.1038/nature06183.

Rohrbach, A., Schmidt, M.W., 2011. Redox freezing and melting in the Earth's deep mantle resulting from carbon–iron redox coupling. Nature 472, 209–212. doi:10.1038/nature09899.

Sato, K., Katsura, T., 2001. Experimental investigation on dolomite dissociation into aragonite + magnesite up to 8.5 GPa. Earth and Planetary Science Letters 184, 529–534. doi:10.1016/S0012-821X(00)00346-0.

Seto, Y., Hamane, D., Nagai, T., Fujino, K., 2008. Fate of carbonates within oceanic plates subducted to the lower mantle, and a possible mechanism of diamond formation. Physics and Chemistry of Minerals 35, 223–229. doi:10.1007/s00269-008-0215-9.

Sieber, M.J., Wilke, M., Appelt, O., Oelze, M., Koch-Müller, M., 2022. Melting relations of Ca–Mg carbonates and trace element signature of carbonate melts up to 9 GPa – a proxy for melting of carbonated mantle lithologies. European Journal of Mineralogy 34, 411–424.

Sinmyo, R., Hirose, K., 2010. The soret diffusion in laser-heated diamond-anvil cell. Physics of the Earth and Planetary Interiors 180, 172–178. doi:10.1016/j.pepi.2009.10.011.

Solopova, N., Dubrovinsky, L., Spivak, A., Litvin, Y.A., Dubrovinskaia, N., 2015. Melting and decomposition of $MgCO_3$ at pressures up to 84 GPa. Physics and Chemistry of Minerals 42, 73–81. doi:10.1007/s00269-014-0701-1.

Stagno, V., Cerantola, V., Aulbach, S., Lobanov, S., McCammon, C.A.,

853 Merlini, M., 2019. Carbon-bearing phases throughout Earth's interior, in:
854 Deep carbon: Past to present. Cambridge University Press, pp. 66–88.

855 Stagno, V., Tange, Y., Miyajima, N., McCammon, C., Irifune, T., Frost,
856 D., 2011. The stability of magnesite in the transition zone and the lower
857 mantle as function of oxygen fugacity. Geophysical Research Letters 38.
858 doi:10.1029/2011GL049560.

859 Takafuji, N., Fujino, K., Nagai, T., Seto, Y., Hamane, D., 2006. Decarbona-
860 tion reaction of magnesite in subducting slabs at the lower mantle. Physics
861 and Chemistry of Minerals 33, 651–654. doi:10.1007/s00269-006-0119-5.

862 Thomson, A., Kohn, S., Bulanova, G., Smith, C., Araujo, D., Walter, M.,
863 2016a. Trace element composition of silicate inclusions in sub-lithospheric
864 diamonds from the Juina-5 kimberlite: Evidence for diamond growth from
865 slab melts. Lithos 265, 108–124. doi:10.1016/j.lithos.2016.08.035.

866 Thomson, A.R., Walter, M.J., Kohn, S.C., Brooker, R.A., 2016b. Slab
867 melting as a barrier to deep carbon subduction. Nature 529, 76–79.
868 doi:10.1038/nature16174.

869 Thomson, A.R., Walter, M.J., Lord, O.T., Kohn, S.C., 2014. Experi-
870 mental determination of melting in the systems enstatite-magnesite and
871 magnesite-calcite from 15 to 80 GPa. American Mineralogist 99, 1544–
872 1554. doi:10.2138/am.2014.4735.

873 Walter, M.J., Bulanova, G., Armstrong, L.S., Keshav, S., Blundy, J.D.,
874 Gudfinnsson, G., Lord, O.T., Lennie, A., Clark, S., Smith, C., et al., 2008.

875 Primary carbonatite melt from deeply subducted oceanic crust. Nature
876 454, 622–625. doi:10.1038/nature07132.

877 Walter, M.J., Thomson, A.R., Smith, E.M., 2022. Geochemistry of silicate
878 and oxide inclusions in sublithospheric diamonds. Reviews in Mineralogy
879 and Geochemistry 88, 393–450. doi:10.2138/rmg.2022.88.07.

880 Wirth, R., Kaminsky, F., Matsyuk, S., Schreiber, A., 2009. Unusual micro-
881 and nano-inclusions in diamonds from the Juina Area, Brazil. Earth and
882 Planetary Science Letters 286, 292–303. doi:10.1016/j.epsl.2009.06.043.

883 Yaxley, G.M., Brey, G.P., 2004. Phase relations of carbonate-bearing eclog-
884 ite assemblages from 2.5 to 5.5 GPa: implications for petrogenesis of
885 carbonatites. Contributions to Mineralogy and Petrology 146, 606–619.
886 doi:10.1007/s00410-003-0517-3.

887 Zhu, F., Li, J., Liu, J., Lai, X., Chen, B., Meng, Y., 2019. Kinetic control
888 on the depth distribution of superdeep diamonds. Geophysical Research
889 Letters 46, 1984–1992. doi:10.1029/2018GL080740.